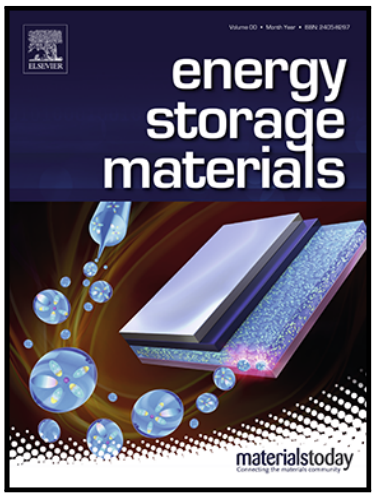

Self-activated cathode substrates in rechargeable zinc–air batteries

Jian Guo , Liqun Kang , Xuekun Lu , Siyu Zhao , Jianwei Li , Paul R. Shearing , Ryan Wang , Dan J.L. Brett , Guanjie He , Guoliang Chai , Ivan P. Parkin

PII: S2405-8297(20)30448-7
DOI: https://doi.org/10.1016/j.ensm.2020.11.036
Reference: ENSM 1430

To appear in: *Energy Storage Materials*

Received date: 20 September 2020
Revised date: 18 November 2020
Accepted date: 25 November 2020

Please cite this article as: Jian Guo , Liqun Kang , Xuekun Lu , Siyu Zhao , Jianwei Li , Paul R. Shearing , Ryan Wang , Dan J.L. Brett , Guanjie He , Guoliang Chai , Ivan P. Parkin , Self-activated cathode substrates in rechargeable zinc–air batteries, *Energy Storage Materials* (2020), doi: https://doi.org/10.1016/j.ensm.2020.11.036

Self-activated cathode substrates in rechargeable zinc–air batteries

Jian Guo,[1, 5] Liqun Kang,[2] Xuekun Lu,[2] Siyu Zhao,[1] Jianwei Li,[1] Paul R. Shearing,[2] Ryan Wang,[2] Dan J.L. Brett,[2] Guanjie He,[1, 2, 4, *] Guoliang Chai[3, *] and Ivan P. Parkin[1, *]

[1]Christopher Ingold Laboratory, Department of Chemistry, University College London, 20 Gordon Street, London WC1H 0AJ, U.K.

[2]Electrochemical Innovation Lab, Department of Chemical Engineering, University College London, London WC1E 7JE, U.K.

[3]State Key Laboratory of Structural Chemistry, Fujian Institute of Research on the Structure of Matter, Chinese Academy of Sciences (CAS), Fuzhou, 350002 Fujian, P.R. China.

[4]School of Chemistry, University of Lincoln, Brayford Pool, Lincoln, LN6 7TS, U.K.

[5]College of Physics, Sichuan University, Chengdu, 610064 Sichuan, P.R. China.

*Correspondence: g.he@ucl.ac.uk (G. He), g.chai@fjirsm.ac.cn (G. Cai), i.p.parkin@ucl.ac.uk (I.P. Parkin)

Acknowledgments

We acknowledge Engineering and Physical Sciences Research Council (EPSRC, EP/L015862/1, EP/R023581/1 and National Natural Science Foundation of China (Grant No. 21703248), STFC Batteries Network (ST/R006873/1), RSC Mobility Grant (M19-7656), Faraday Institution (EP/S003053/1) Degradation project (FIRG001) and the Strategic Priority Research Program of the Chinese Academy of Sciences (Grant No. XDB20000000) for funding support, E01 and E02 beamline of electron Physics Science Imaging Centre (ePSIC) in Diamond Light Source (DLS) for the allocated experiment session EM22572 and EM20847. J. Guo would like to thank the University College London and China Scholarship Council for a joint UCL-CSC PhD scholarship.

Abstract

Developing cost-effective and durable air-cathodes is crucial for improving metal-air batteries. Most reports of cathode formulation involve preparing bi-functional electrocatalysts

from wet chemistry or solid-state synthesis, followed by pasting onto a substrate. In this work, the cathodes generated from electrochemical activation of normal carbon paper substrates were directly used in Zn-air batteries. The self-activated carbon paper substrate without any additional electrocatalysts exhibits an impressive cycling stability (more than 165 hours for 1,000 cycles) and a small discharge-charge voltage gap. After the activation, the maximum power density and electrochemical surface area were increased by over 40 and 1,920 times respectively. It is discovered that substrates after activation can be directly used as a cathode. The new method is scalable, inexpensive and produces near best in class performance. The mechanism behind this enhancement is due to the creation of oxygen functional groups within the cathode, which overcame slow kinetics, enhanced wettability and enabled optimum three-phase boundaries.

Keywords: self-activation, carbon paper substrates, oxygen functional groups, air-cathodes, zinc-air batteries

1. Introduction

Sustainable energy sources and devices have attracted tremendous attention from both academia and industry in the past decade due to environmental concerns and a switch from fossil fuel to renewables.[1] Fuel cells and metal-air batteries are used for applications such as electric vehicles, wearable electronic devices and grid-scale energy storage stations. Among which, Zn-air batteries (ZABs) have the advantage of low-cost (currently <\$100 kWh^{-1}, and potentially <\$10 kWh^{-1}) and high theoretical energy density (1,084 Wh kg^{-1}),[2–4] intrinsic safety, low toxicity and high natural abundance and ready availability of Zn.[3,5–7] However, the specific capacity and energy efficiency are severely restricted by the sluggish kinetics of the oxygen reduction reaction (ORR) and oxygen evolution reaction (OER) occurring at air-cathodes.[8] Most studies in ZABs focus on the development of cost-effective and high performance electrocatalysts for ORR and OER.[9–15] Significant progress has been achieved over the past ten years which can be reflected from the sharply increased number of publications around ZABs (Fig. S1).

Noble-metal ORR/OER catalysts such as Pt/C, Pt-Co, Pt-Ni, PdMo and Ru/IrO_2 set the benchmark for air-cathode performance yet are expensive;[15–19] however, modified carbon materials and transition metal derivatives (single atoms or metal oxides/sulfides/nitrides) have been demonstrated as promising replacement candidates.[20–28] In carbon-based metal-free

structures, most of studies have focused on the development of N, S and P doped carbon,[29–33] because these rationally introduced heteroatoms into the carbon materials can lead to spin and charge redistribution in the sp^2 carbon lattice and break the original electroneutrality, which create active sites for both OER and ORR.[8] Recently, a few publications have reported that oxygen doped carbon materials can function as air-cathodes for ZABs.[1,8,34] Compared with other heteroatoms, oxygen functional groups can be introduced into the carbon matrix easily by just using water or air under mild conditions;[8] however, the detailed mechanism of oxygen-induced performance improvement of carbon electrocatalysts is yet to be resolved. Moreover, to fabricate air-cathodes in ZABs, these electrocatalysts are normally mixed with polymer binders and coated on conductive substrates, such as carbon paper, nickel foam and stainless-steel mesh, to generate gas diffusion layers and facilitate the electron and oxygen gas mass transfer.[1,8] But the durability, uniformity and reproducibility of the as-prepared air-cathodes are variable and depend on the materials and electrode fabrication processes in different laboratories.[34] Therefore, for the fabrication of practical devices, it is desirable to simplify the process by integrating active catalysts with the substrates *in-situ*. Recently, acid oxidation, high temperature hydrogen etching, water treatment and plasma techniques have been successfully implemented to create surface oxygen functional groups on graphite and carbon cloth materials.[1,8,34,35] As a result, these activated carbon materials exhibited enhanced ORR and OER performance. Nevertheless, the processing of these materials involves strong acid oxidation and high temperature carbonization in the presence of highly flammable H_2 gas, which is complex and has safety issues. In addition, studies tend to focus on the design of rational electrocatalysts, with the effect and contribution from the substrate, especially during and after electrochemical processes, are generally ignored.

We herein discovered the self-activation phenomenon of carbon paper (CP) cathode substrates during the galvanostatic discharge-charge (GDC) process in ZABs. During this facile process, the commercial CP can be easily activated to generate porous and reduced hydrophobic surfaces with abundant functional groups and a dramatically enhanced electrochemical surface area. Consequently, the self-activated CP when used directly as an air-cathode without any further treatment, exhibits impressive cycling stability (more than 165 hours over 1000 cycles) and a small charge-discharge voltage gap (0.99 V) at a current density of 2.5 mA cm^{-2} in ZABs, which is comparable to, or even better than, many reported metal-free or metal/oxide nanostructure grafted carbon-based electrocatalysts that adopt complicated synthetic procedures (Table S7). Combined *ex-situ* characterization and multi-scale

simulations detected the structural evolution of the air-cathodes and a structure-performance relationship was established.

2. Results and discussion

The self-activation phenomenon induced performance improvement is shown in Fig. 1A-C (individual battery cycling performance in Fig. S2), the commercial PTFE coated CP was used directly as air-cathode in ZABs for GDC cycling tests under current densities at 1, 2.5 and 5 mA cm^{-2}, respectively. In the initial 5 hours, a dramatic decrease in the charge voltage and increase of the discharge voltage was observed, which induced a sharply reduced voltage gap. After about 10 hours of continuous discharge-charge activation, the charge voltage, discharge voltage and the voltage gap became stable. The changes of the CP surface morphology after 50 hours of discharge-charge cycling activation at different current densities were revealed by scanning electron microscopy (SEM). A current density dependent PTFE etching effect on surface can be seen in Fig. 1D-G (Fig. S3). With an increased current density during the activation period, the surface PTFE etching effect becomes more obvious with more raw carbon fibres exposed to the electrolyte. The evolution of hydrophobicity of the CP surface was further elucidated by water contact angle (CA) measurements, as shown in the inset of Fig. 1D-G. With an increase of the current densities, the surface wettability improved after the same activation period. An evident change of surface wettability and pore structure after the self-activation process indicates that the optimized surface of the CP is more favorable for the permeation of the electrolyte and diffusion of oxygen, also resisting excessive invasion from water and constructing stable gas/liquid/solid triple-phase boundaries.[4] Further structural characteristics of the original CP and self-activated CP were compared by X-ray diffraction (XRD), Raman spectroscopy and Fourier transform infrared spectroscopy (FTIR). During the GDC cycling process, the surface PTFE polymer was gradually eroded, as indicated by the decrease of its characteristic peak intensity from the XRD (Fig. 1H and Fig. S3I). The gradually increased I_G/I_D ratio with respect to the activation current densities and increasingly obvious 2D band in the Raman spectra confirmed the surface PTFE etching effect and concomitant exposure of the graphitic carbon fibres (Fig. 1I). The FTIR spectra in Fig. 1J showed that only two strong peaks appear in the original CP, which can be allocated to symmetrical (1200 cm^{-1}) and asymmetrical (1145 cm^{-1})

stretching modes of $–CF_2$.[36] After being activated with different current densities, additional bands emerged, which can be assigned to the stretching vibrations of carboxylate ions COO^- (1620 cm^{-1} and 1390 cm^{-1}), O–H bending (1365 cm^{-1}), C–O stretching (1005 cm^{-1}) and C=C bending (829 cm^{-1} and 700 cm^{-1}), respectively.[8] These results are consistent with the above analyses, and further suggest the existence of oxygen functional groups in the self-activated CP. Therefore, the corrosion effect of the electrolyte, the weak adhesion of PTFE on the carbon fibres and the oxygen evolution related gas expansionary force lead to the etching and partial exfoliation of PTFE from the surface of carbon fibres, causing an optimized triple-phase boundary. Then, the exposed carbon fibres can provide better electron transfer pathway and rich accessibility of electrolytes to achieve efficient oxygen evolution reaction and result in surface oxidized activated CP with abundant oxygen functional groups.

Further insights on the transformation of surface and bulk composition of self-activated CP compared with the original CP were investigated by X-ray photoelectron spectroscopy (XPS) and energy dispersive X-ray spectroscopy (EDS). As expected, the SEM-EDS spectrum and XPS survey spectra analyses indicate that the surfaces of all CP cathodes are composed mainly of carbon and fluorine (Fig. S4-S9 and Table S1). The GDC cycling process can effectively introduce oxygen functional groups on the surface of CP, and the surface oxygen content increases with the increase of the activation current densities from 0.00 atom% for original CP to 5.85, 7.01 and 8.52 atom% for self-activated CP at 1, 2.5 and 5 mA cm^{-2}, respectively (Fig. S4). More specifically, the high-resolution C 1s XPS spectra of self-activated CP can be deconvoluted into nine regions. The peak at 283.5 eV originates from the neighbouring lattice vacancies of carbon atoms,[37] and the peaks located at 284.6 eV and 285.3 eV can be attributed to the delocalized and localized hydrocarbons (Fig. 2A). The peaks at higher binding energies correspond to the oxidized carbon in the form of oxygen functional groups on the surface of self-activated CP: C–OH (285.8 eV), C=O (286.8 eV) and COOH (288.2 eV) (Fig. 2A and Table S2).[38] The high-resolution O 1s XPS spectra of self-activated CP can be fitted into carbonyl (C=O) groups at 530.8 eV, hydroxyl (C–OH) groups at 532.0 eV, ester (O–C=O) groups at 533.4 eV and carboxyl (–COOH) groups at 534.4 eV, respectively (Fig. 2B and Table S3)[39] The variations of oxygen content derived from XPS and EDS are summarized in Fig. 2C, these comprehensive analyses clearly illuminated that the major change between the original and self-activated CP was the introduction of rich oxygen functional groups on the surface of CP, especially the increased amount of carbonyl, hydroxyl and carboxyl groups.

To further understand the differences in fine electronic structure of surface species of the original and self-activated CP, near-edge X-ray absorption fine structure spectroscopy (NEXAFS) was conducted. Fig. 2D shows the C K-edge NEXAFS spectra of the original CP and self-activated CP at 2.5 mA cm^{-2}. For the self-activated CP electrode, two additional absorption peaks could be found at 297.2 and 299.8 eV, which are attributed to the electron transition of potassium $2p_{3/2}$ to σ* and $2p_{1/2}$ to σ*, respectively. The absorption peak of K L_3-edge and K L_2-edge indicates the trace amount of potassium on the surface. The enhanced peak at about 292.5 eV reflects the planar sp^2 hybridization of the valence 2s and $2p_{xy}$ states of carbon (fingerprints of the trigonal coordination of carbon atoms in graphite). The assessments of absorption peaks are listed in the Table S4 and the peak fitting results are shown in Fig. S10. The formation of new oxidized carbon species could be deduced. Besides, the O K-edge NEXAFS spectra can be divided into two regions: the sharp pre-edge features below 535 eV and the broad absorption peak at higher energy (Fig. 2E and Fig. S11). The pre-edge features in O K-edge NEXAFS spectra originate from electron transitions of O 1s core levels to 2p π* states, representing the hybridization of O 2p and C 2p orbitals (ketone/carboxyl group C=O bond). The high energy humps are attributed to σ*(C=O) from ketone/carboxyl/alcoholic hydroxyl. The additional peak in self-activated CP at 533.4 eV can be ascribed to 1s to σ* transition of alcohol (C–OH)/ether (C–O–R). Therefore, after the self-activation, new C–O species are formed. Furthermore, the high-angle annular dark-field scanning transmission electron microscopy (HAADF-STEM) was used to display the high-magnification nanostructures of the self-activated CP. The distinct contrast shows the stacked graphitic carbon layers, which is normal for commercial CP frameworks. The presence of homogeneous distribution of oxygen doping in self-activated CP is further verified by STEM-EDS and SEM-EDS elemental mapping analysis (Fig. 2F and Fig. S12). Furthermore, considerable amount of K and trace Zn elements can be detected, resulting from the residue in the electrolyte.

Multiscale simulations were carried out to examine the self-activated CP from atomic to electrode scales for uncovering the origins of the self-activation phenomenon and the enhanced energy conversion ability. Firstly, the atomic-scale simulations were performed to investigate the perspective ORR/OER active sites and mechanisms of the carbon-based electrocatalysts. Carbon materials with –O, –OH, –COOH, –F, $–CF_3$, or Zn related structures are shown in Fig. 3A. The free energy variations between *O, *OH and *OOH intermediates were calculated by DFT simulations to obtain electrochemical potentials.[40–42] The

calculated ORR/OER electrochemical potentials are shown in Fig. 3B-D. It is noted that the ORR/OER potentials are 0.54/2.0 V for an undoped carbon edge. The ORR potential is increased to 0.61 V when the edge is decorated with –COOH group, and the OER potential is decreased to 1.69 V when the edge is decorated with –OH group. Both two potentials are the optimized values from the theoretical calculation. Therefore, the –OH or –COOH group decoration should improve the ORR/OER performance for the O_2 electrode. For the –O group decorated edge, the ORR potential is decreased to 0.21 V, and the OER potential is as high as 2.71 V, which indicates that the –O group is unfavourable for ORR/OER. The ORR/OER potentials for –F (–CF_3) decorated edges are 0.21(0.29) V/1.79(1.81) V. The –F related structures can improve the OER performance while that for ORR is decreased. Finally, the ORR/OER potentials for the Zn related structure are 0.01 V/3.16 V, which shows rather notorious ORR/OER performance. As the –OH/–COOH related structures may deliver improved ORR/OER performance, the free energy variations for the ORR process on the –COOH related structure, and that for the OER process on the –OH related structure are shown in Fig. 3C-D. It can be clearly seen that the rate-determining step for ORR on the –COOH related structure is the removal of *OH intermediates at the last elementary step. The rate-determining step for the OER on the –OH related structure is the second elementary step that forming *O intermediates. Moreover, as shown in Fig. S13, the K and Zn doped structures are unfavorable for ORR and OER. The ORR and OER potentials for the catalysts with mixed two different metal free groups are also studied and shown in Fig. S14 and Fig. S15. The results indicate that the ORR and OER potentials only slightly change compared with one group doped carbon materials catalysts.

It is well-known that the performance of air-cathodes is mainly determined by the combination of exposed active sites, electrical conductivity and mass transport.[43] Performance at higher current densities was particularly influenced by mass transport of oxygen through the electrode structure. To gain insight into this aspect of operation of the self-activated CP electrode, computational fluid dynamics (CFD) simulation was performed on the entire electrode (bottom) and the reaction-active zone (upper) respectively (Fig. 3E). The inlet boundary condition was set to an air pressure of 1 bar and a reaction source was defined at the outlet equivalent to 3 mA in the entire electrode simulation. It displays that due to the coarse pore structure in the carbon fibre layer, the gas flow primarily through the major connected channels, compared to that in the reactive zone, where the flow distribution is more homogeneous as a result of the evenly distributed finer pore structure (shown by the slices

inset). A second simulation solely in the reactive region shows that the mass flux (coloured in orange) spread across the whole reaction layer. The obtained tortuosity from the CFD simulation in the reactive zone is slightly higher than the entire electrode, which is attributed to the loss of pore connectivity and slightly lower porosity in the reactive zone. However, this loss in mass transport property is negligible compared to the improved reaction kinetics benefit from the electrochemical self-activation treatment. The hierarchical pore structure is beneficial and widely used in the material design for energy conversion and storage devices.[44,45]

The above results clearly demonstrated the self-activation effect in CP cathode substrate for ZABs during the GDC cycling process. However, it is still worthy to further clarify the generation of this phenomenon by separating contribution of discharge and charge processes. Therefore, additional experiments on independent discharge and charge followed with cycling tests were conducted to investigate the relationship between the two separate process and related structural change of the CP. Firstly, individual 10-hour charge and discharge followed with 300 cycles discharge-charge cycling experiments were performed to compare their different contribution. As shown in Fig. S16, the cycling performance was very stable after 10-hour charge. However, after 10-hour discharge, a self-activation phenomenon still can be observed in the initial a few hours of the following cycling performance, which indicates that the 10-hour charge process is more effective than discharge process to realize the self-activation. The related compositional and structural differences between 10-hour charge and 10-hour discharge samples were revealed by XPS spectra and SEM-EDS analyses (Fig. S17-S23 and Table S5). Subsequently, as the charge curve reached a saturated state within 4 hours (Fig. S16A), independent 3.5-hour charge and discharge followed with 300 cycles discharge-charge cycling were performed to further confirm the different effect of charge and discharge process (Fig. S24-S32). Overall, the charge process can be more effective to etch the surface PTFE polymer compared with discharge process and generate more oxygen functional groups on the surface of CP (Fig. S29 and Fig. S30, Table S6). Therefore, compared with the 3.5-hour discharge, after only 3.5-hour charge, the self-activated CP can boost battery performance and enhanced peak power density (Fig. S24 and Fig. S25).

Based on the above systematic analyses, it was recognized that the self-activated CP can be directly used as an efficient self-standing air-cathode in a rechargeable ZAB, as illustrated in Fig. 4A. The self-activated CP shows an increased and stable open-circuit voltage at 1.35V (Fig. S33), and the peak power density of the self-activated CP is more than 40 times higher

than the original CP (Fig. 4B and Fig. S34). The slight open-circuit voltage change may due to modest differences among standing time of cells and lab conditions. The electrochemically active surface area (ECSA) of the original CP compared to the self-activated CP were estimated by measuring the double layer capacitance (C_{DL}) in a non-faradaic potential window. Impressively, after a simple electrochemical activation, the C_{DL} of the self-activated CP is dramatically enhanced by 1921 times to 19.21 mF cm^{-2}, compared with 0.01 mF cm^{-2} for the original CP (Fig. 4C and Fig. S35). The remarkable ECSA enhancement of self-activated CP could be due to the combined effects of the increased amount of oxygen functional groups on CP surface and a porous and reduced hydrophobic surface structure, which further confirmed the advantage of the electrochemical self-activation process since a larger ECSA plays a crucial role in enhancing the overall electrocatalytic activities.[8,46]

The galvanostatic discharge curve at a current density of 2.5 mA cm^{-2} shows a discharge potential of 1.02 V for the ZAB with the self-activated CP as an air-cathode, and with negligible decrease of the discharge potential after 30 hours. The calculated specific capacity during discharge is 571 mAh g^{-1} for the ZAB with self-activated CP as air cathode (Fig. S36), which is even higher than the reported benchmark IrO_2 + Pt/C catalysts coated on the carbon paper (499 mAh g^{-1}).[18] In a proof-of-principle demonstration to show practical application, a single ZAB with self-activated CP as the air-cathode was used to power a digital thermo-hygrometer (Fig. 4D). To further demonstrate the rechargeability and durability of the ZAB based on self-activated CP as air-cathodes, additional 1000 cycles of GDC measurements were performed at a current density of 2.5 mA cm^{-2} (Fig. 4E). The ZAB with self-activated CP as the air-cathode exhibits a stable discharge and charge potential at 1.06 V and 2.05V, respectively. The charge/discharge voltage gap is 0.99 V, with a round-trip efficiency of 51.7%, which is comparable to the commercial noble metal-based catalysts and many other state-of-the-art catalysts (Table S7), the formation of a turning point in the galvanostatic charge-discharge curves after a certain cycles could be due to the side reaction of further oxidization of the graphitic carbon and the reduction of electrolyte conductivity *via* forming carbonate between the KOH and CO_2 after long-term galvanostatic cycling test without replacing the electrolyte and zinc plate.[8,34] To further demonstrate the universality of the self-activation effect in cathode substrates in ZABs, another frequently-used hydrophobic nickel foam was used as an air-cathode directly to undergo galvanostatic cycling test. A similar self-activation phenomenon can be observed, after GDC cycling tests, the activated nickel foam as an air-cathode shows an obvious enhanced performance in terms of charge/discharge voltage gap and peak power density for ZABs (Fig. S37 and Fig. S38).

3. Conclusion

In summary, a self-activation effect on common carbon cathode substrates in ZABs was observed and reported for the first time. The experimental and simulation analyses reveal that the enhanced electrocatalytic performance can be attributed to the improved wettability with optimized three-phase boundaries, oxygen-rich functional groups as active species and a dramatically enhanced electrochemical surface area, with trivial loss of mass transport capability owing to the formed hierarchical pore structure. This work paves a pathway for multiscale and synergistic engineering and designing of efficient self-standing air-cathodes for metal-air batteries by an extremely facile and low-cost method. It is believed that monitoring not only the behaviours of electrode materials/electrocatalyst but also the current collectors/gas diffusion layers during electrochemical process are necessary for rational design of high-performance devices. Future investigation will focus on *in-situ* characterisation of the interaction of electrode materials/current collectors from chemistry and physics perspectives, as well as the engineering of electrodes and devices to optimize the overall performance.

4. Experimental section

Materials

Carbon paper (TGP-H-060 hydrophobic, State Power Investment Corporation Limited), potassium hydroxide (KOH), ≥85%, pellets (Alfa Aesar), zinc acetate dihydrate ($Zn(CH_3COO)_2 \cdot 2H_2O$, Alfa Aesar), zinc plate (purity: 99.9%, thickness: 0.5mm), 1H,1H,2H,2H-perfluorooctyltriethoxysilane ($C_8F_{13}H_4Si(OCH_2CH_3)_3$, 97%, Alfa Aesar), nickel foam (MTI Corporation).

Preparation of self-activated CP

The commercial PTFE treated CP was directly used as an air-cathode in a Zn-air battery for galvanostatic discharge-charge cycling tests with current densities of 1 mA cm^{-2}, 2.5 mA cm^{-2} and 5 mA cm^{-2}, respectively. The self-activated CP was obtained after 300 cycles galvanostatic discharge-charge cycling. The cycling tests were performed for 10 min per cycle (discharge: 5 min; charge: 5 min).

Preparation of hydrophobic nickel foam cathode

150 μL of 1H,1H,2H,2H-perfluorooctyltriethoxysilane was placed into 25mL of absolute ethanol, and the solution was stirred for 2 hours. Then, a piece of nickel foam (3.5×3.5 cm^2) was immersed into the solution for ~ 3 min. Finally, the nickel foam was dried in air overnight and used as the hydrophobic nickel foam cathode.

Structural Characterization

X-ray diffraction (XRD, Cu-K-α, λ = 1.54184 Å) was carried out by using a Bruker-Axs D8 X-ray diffractometer. The reference database card for XRD analysis is Graphite-2H (JCPDS No. 41-1487). Raman spectroscopy (514.5 nm laser, Renishaw) was carried out by placing samples on a glass slide. FT-IR data was obtained by Bruker ALPHA FTIR Spectrometer (Platinum-ATR) with background correction. Scanning electron microscopy, SEM-EDS spectrum analysis and elemental mapping (SEM, ZEISS EVO MA10) were carried out by pasting the samples on a carbon tape. Annular Bright Field and High Angle Annular Dark Field Scanning Transmission Electron Microscopy (BF-STEM and HAADF-STEM) characterizations were performed on a probe-corrected (CEOS) JEM ARM 200CF (JEOL, Japan) operated at 200 keV and probe-corrected (JEOL-COSMO) JEM ARM 300CF (JEOL, Japan) operated at 300 keV. A 30 μm probe-forming aperture was applied, result in 26.2 convergence semi-angle. The ABF and HAADF signals were gathered at 9.0 cm camera length, integrating the scattered electrons from 12.6 to 27.7 mrad and from 77 to 209 mrad, respectively. Energy-Dispersive X-ray Spectroscopy (EDS) and elemental mapping data were obtained *via* the JEM ARM 200CF equipped large solid-angle dual EDS detectors. Each EDS spectrum image is 100 × 100 pixels in size with 0.05 second exposure time per pixel. A drifting correction was applied every 30 seconds during the EDS data acquisition process. Gatan Microscopy Suite Software was used for both STEM imaging and EDS spectrum acquisition. Contact angle (CA) measurements were performed at ambient temperature with 7 μL water droplet as the indicator (FTA-1000 drop shape instrument, First Ten Angstroms Inc.). X-ray Photoemission spectroscopy (XPS) tests were carried out by Al-K-α, Thermo Fisher Scientific.

The C K-edge and O K-edge near-edge X-ray absorption fine structure (NEXAFS) measurements were performed at the BL12b bending magnet beamline in the Heifei Advanced Light Source. NEXAFS data was acquired in Total Electron Yield (TEY) mode *via* measuring the sample drain current. All NEXAFS spectrum were analysed by Athena (included in Demeter software package, version 0.9.26) for background removal, normalization and peak fitting. For multi-length scale X-ray computed tomography (X-ray

CT), a 2 mm diameter disk was first extracted from the electrode sheet using an A Series/Compact Laser Micromachining System (Oxford Laser, Oxford, UK) and mounted onto the sample holder and put into the lab-based X-ray computed-tomography microscope (Zeiss Xradia Versa 520). A total number of 2401 projections were sequentially acquired at the acceleration voltage of 80 kV over a 360° rotation with an exposure time of 3 seconds/frame. The sample-to-source and sample-to-detector distance were adjusted to obtain the voxel resolution of 1 μm. Built-in Feldkamp-Davis-Kress (FDK) algorithm[47] was used for the reconstruction (Zeiss XMReconstructor, Carl Zeiss X-ray Microscopy Inc., Pleasanton, CA). The post analysis was conducted using commercial software Avizo V9.5 (ThermoFisher Scientific).

Assembly and electrochemical measurements of Zn-air batteries

Zn-air battery performances in two-electrode configuration were analyzed on commercial Zn-air battery cells. Typically, the air-cathode was prepared by using a fresh carbon paper (or hydrophobic nickel foam) attached with a gas diffusion layer on the backside. A piece of polished Zn plate was used as the anode, and 6.0 M KOH with 0.2 M $Zn(CH_3COO)_2{\cdot}2H_2O$ was prepared as the electrolyte for the reversible electrochemical reactions. All the designed batteries were tested under atmospheric conditions. The galvanostatic discharge-charge cycling and galvanostatic discharge tests were conducted on a NEWARE CT4008 multichannel battery testing system. The cycling tests were performed for 10 min per cycle (discharge: 5 min; charge: 5 min) at a pre-set current density. The polarization curves and cyclic voltammetry (CV) scans of the as-fabricated Zn-air batteries were measured with Gamry Interface 1010E Potentiostat. Electrochemical active surface area (ECSA) was determined by measuring the capacitive current associated with double-layer charging from the scan-rate dependence of CV. The CV scans were performed in a potential range between 1.32 and 1.40 V at different scan rates of 1, 2, 5, 10, and 20 mV s^{-1}. Then the electrochemical capacitance of the electrodes was estimated by linear fitting of the charging and discharging current density differences ($\Delta j = j_a - j_c$ at a potential of 1.36 V) against the scan rate. The slope is twice of the double layer capacitance (C_{DL}), which is used to evaluate ECSA. The energy efficiency was calculated from the ratio of discharge to charge voltages. The specific capacities were determined using the galvanostatic discharge profiles standardized to the consumed mass of Zn.

The density functional theory (DFT) simulation

The density functional theory (DFT) simulations for ORR and OER were performed by using PWSCF code in Quantum ESPRESSO suite.[48] The exchange correlation functional was described by the generalized gradient approximation of Perdew-Burke-Ernzerhof (GGA-PBE).[49] The kinetic cut-off energies for the wavefunction and the charge are set to 35 Ry and 350 Ry, respectively. The carbon material catalysts with –O, –OH, –COOH, –F, $–CF_3$, or Zn related structures are shown in Fig. 3A. The free energy variations for each electrochemical step are calculated as previous papers.[41,42,50]

Computed Fluid Dynamics (CFD) simulation

The reconstructed 3D electrode was first segmented into active material and air using greyscale thresholding method, and then converted into surface mesh (.stl format) to be imported into commercial CFD software Star-CCM+ (CD-Adapco Inc., London). A mesh refinement step was first undertaken to reduce the total mesh number by replacing the tetrahedral element with polyhedral element. Air at ambient pressure was assigned as the boundary condition at the inlet and a constant oxygen consumption (1.5 A cm^{-2}) at the electrolyte/electrode interface was applied. The computation of the tortuosity factor of the porous structure is well explained elsewhere.[44]

Declaration of interests

The authors declare no conflicts of interests.

APPENDIX A. Supporting information

Supplementary data associated with this article can be found in the online version.

CRediT Author

Jian Guo: Conceptualization, Data curation, Writing-Original draft preparation; **Liqun Kang:** Formal analysis, Methodology, Writing-Original draft preparation; **Xuekun Lu:** Formal analysis, Methodology, Data Curation, Writing-Original draft preparation; **Siyu Zhao:** Data Curation; **Jianwei Li:** Data Curation; **Paul R. Shearing:** Formal analysis; **Ryan Wang:** Data Curation; **Dan J.L. Brett:** Funding acquisition, Writing-Review & Editing; **Guanjie He:** Conceptualization, Methodology, Funding acquisition, Supervision, Writing-Review & Editing; **Guoliang Chai:** Conceptualization, Funding acquisition, Writing-Review & Editing; **Ivan P. Parkin:** Supervision, Funding acquisition, Writing-Review & Editing

Graphical abstract

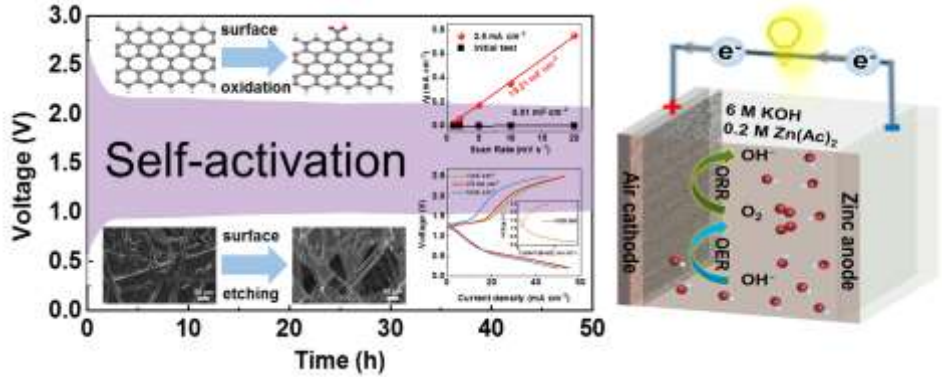

References

[1] Z. Liu, Z. Zhao, Y. Wang, S. Dou, D. Yan, D. Liu, Z. Xia, S. Wang, In Situ Exfoliated, Edge-Rich, Oxygen-Functionalized Graphene from Carbon Fibers for Oxygen Electrocatalysis, Adv. Mater. 29 (2017) 1606207. https://doi.org/10.1002/adma.201606207.

[2] F. Cheng, J. Chen, Metal-air batteries: From oxygen reduction electrochemistry to cathode catalysts, Chem. Soc. Rev. 41 (2012) 2172–2192. https://doi.org/10.1039/c1cs15228a.

[3] J.S. Lee, S.T. Kim, R. Cao, N.S. Choi, M. Liu, K.T. Lee, J. Cho, Metal-air batteries with high energy density: Li-air versus Zn-air, Adv. Energy Mater. 1 (2011) 34–50. https://doi.org/10.1002/aenm.201000010.

[4] T. Zhou, N. Zhang, C. Wu, Y.Xie, Surface/interface nanoengineering for rechargeable Zn–air batteries, Energy Environ. Sci. 13 (2020) 1132–1153. https://doi.org/10.1016/0025-326X(83)90196-0.

[5] Y. Li, M. Gong, Y. Liang, J. Feng, J.E. Kim, H. Wang, G. Hong, B. Zhang, H. Dai, Advanced zinc-air batteries based on high-performance hybrid electrocatalysts, Nat. Commun. 4 (2013) 1805. https://doi.org/10.1038/ncomms2812.

[6] Y. Li, H. Dai, Recent advances in Zinc-air batteries, Chem. Soc. Rev. 43 (2014) 5257–5275. https://doi.org/10.1039/c4cs00015c.

[7] P. Tan, B. Chen, H. Xu, H. Zhang, W. Cai, M. Ni, M. Liu, Z. Shao, Flexible Zn- and Li-air batteries: Recent advances, challenges, and future perspectives, Energy Environ. Sci. 10 (2017) 2056–2080. https://doi.org/10.1039/c7ee01913k.

[8] K. Kordek, L. Jiang, K. Fan, Z. Zhu, L. Xu, M. Al-Mamun, Y. Dou, S. Chen, P. Liu, H. Yin, P. Rutkowski, H. Zhao, Two-Step Activated Carbon Cloth with Oxygen-Rich Functional Groups as a High-Performance Additive-Free Air Electrode for Flexible Zinc–Air Batteries, Adv. Energy Mater. 9 (2019) 1802936.

https://doi.org/10.1002/aenm.201802936.

[9] Y. Jiao, Y. Zheng, M. Jaroniec, S.Z. Qiao, Design of electrocatalysts for oxygen- and hydrogen-involving energy conversion reactions, Chem. Soc. Rev. 44 (2015) 2060–2086. https://doi.org/10.1039/C4CS00470A.

[10] S. Fu, C. Zhu, J. Song, D. Du, Y. Lin, Metal-Organic Framework-Derived Non-Precious Metal Nanocatalysts for Oxygen Reduction Reaction, Adv. Energy Mater. 7 (2017) 1700363. https://doi.org/10.1002/aenm.201700363.

[11] X. Cai, L. Lai, J. Lin, Z. Shen, Recent advances in air electrodes for Zn-air batteries: Electrocatalysis and structural design, Mater. Horizons. 4 (2017) 945–976. https://doi.org/10.1039/c7mh00358g.

[12] J. Fu, Z.P. Cano, M.G. Park, A. Yu, M. Fowler, Z. Chen, Electrically Rechargeable Zinc–Air Batteries: Progress, Challenges, and Perspectives, Adv. Mater. 29 (2017) 1604685. https://doi.org/10.1002/adma.201604685.

[13] H.F. Wang, C. Tang, Q. Zhang, A Review of Precious-Metal-Free Bifunctional Oxygen Electrocatalysts: Rational Design and Applications in Zn−Air Batteries, Adv. Funct. Mater. 28 (2018) 1803329. https://doi.org/10.1002/adfm.201803329.

[14] J. Pan, Y.Y. Xu, H. Yang, Z. Dong, H. Liu, B.Y. Xia, Advanced Architectures and Relatives of Air Electrodes in Zn–Air Batteries, Adv. Sci. 5 (2018) 1700691. https://doi.org/10.1002/advs.201700691.

[15] C. Han, W. Li, H.K. Liu, S. Dou, J. Wang, Design strategies for developing non-precious metal based bi-functional catalysts for alkaline electrolyte based zinc-air batteries, Mater. Horizons. 6 (2019) 1812–1827. https://doi.org/10.1039/c9mh00502a.

[16] L. Chong, J. Wen, J. Kubal, F.G. Sen, J. Zou, J. Greeley, M. Chan, H. Barkholtz, W. Ding, D.J. Liu, Ultralow-loading platinum-cobalt fuel cell catalysts derived from imidazolate frameworks, Science 362 (2018) 1276–1281. https://doi.org/10.1126/science.aau0630.

[17] X. Tian, X. Zhao, Y.Q. Su, L. Wang, H. Wang, D. Dang, B. Chi, H. Liu, E.J.M. Hensen, X.W. Lou, B.Y. Xia, Engineering bunched Pt-Ni alloy nanocages for efficient oxygen reduction in practical fuel cells, Science 366 (2019) 850–856. https://doi.org/10.1126/science.aaw7493.

[18] M. Luo, Z. Zhao, Y. Zhang, Y. Sun, Y. Xing, F. Lv, Y. Yang, X. Zhang, S. Hwang, Y. Qin, J.Y. Ma, F. Lin, D. Su, G. Lu, S. Guo, PdMo bimetallene for oxygen reduction catalysis, Nature. 574 (2019) 81–85. https://doi.org/10.1038/s41586-019-1603-7.

[19] L. Wang, Z. Zeng, W. Gao, T. Maxson, D. Raciti, M. Giroux, X. Pan, C. Wang, J.

Greeley, Tunable intrinsic strain in two-dimensional transition metal electrocatalysts, Science 363 (2019) 870–874. https://doi.org/10.1126/scienceaat8051.

[20] G. Wu, K.L. More, C.M. Johnston, P. Zelenay, High-performance electrocatalysts for oxygen reduction derived from polyaniline, iron, and cobalt, Science 332 (2011) 443–447. https://doi.org/10.1126/science.1200832.

[21] Z.W. Seh, J. Kibsgaard, C.F. Dickens, I. Chorkendorff, J.K. Nørskov, T.F. Jaramillo, Combining theory and experiment in electrocatalysis: Insights into materials design, Science 355 (2017) eaad4998. https://doi.org/10.1126/science.aad4998.

[22] Y. Chen, S. Ji, C. Chen, Q. Peng, D. Wang, Y. Li, Single-Atom Catalysts: Synthetic Strategies and Electrochemical Applications, Joule. 2 (2018) 1242–1264. https://doi.org/10.1016/j.joule.2018.06.019.

[23] L. Liu, A. Corma, Metal Catalysts for Heterogeneous Catalysis: From Single Atoms to Nanoclusters and Nanoparticles, Chem. Rev. 118 (2018) 4981–5079. https://doi.org/10.1021/acs.chemrev.7b00776.

[24] L. Ma, Y. Zhao, X. Ji, J. Zeng, Q. Yang, Y. Guo, Z. Huang, X. Li, J. Yu, C. Zhi, A Usage Scenario Independent "Air Chargeable" Flexible Zinc Ion Energy Storage Device, Adv. Energy Mater. 9 (2019) 1900509. https://doi.org/10.1002/aenm.201900509.

[25] Y.P. Deng, Y. Jiang, R. Liang, S.J. Zhang, D. Luo, Y. Hu, X. Wang, J.T. Li, A. Yu, Z. Chen, Dynamic electrocatalyst with current-driven oxyhydroxide shell for rechargeable zinc-air battery, Nat. Commun. 11 (2020) 1952. https://doi.org/10.1038/s41467-020-15853-1.

[26] Z. Pei, Y. Huang, Z. Tang, L. Ma, Z. Liu, Q. Xue, Z. Wang, H. Li, Y. Chen, C. Zhi, Enabling highly efficient, flexible and rechargeable quasi-solid-state zn-air batteries via catalyst engineering and electrolyte functionalization, Energy Storage Mater. 20 (2019) 234–242. https://doi.org/10.1016/j.ensm.2018.11.010.

[27] Y. Jiang, Y.P. Deng, R. Liang, J. Fu, D. Luo, G. Liu, J. Li, Z. Zhang, Y. Hu, Z. Chen, Multidimensional Ordered Bifunctional Air Electrode Enables Flash Reactants Shuttling for High-Energy Flexible Zn-Air Batteries, Adv. Energy Mater. 9 (2019) 1900911. https://doi.org/10.1002/aenm.201900911.

[28] G. He, X. Han, B. Moss, Z. Weng, S. Gadipelli, F. Lai, A.G. Kafizas, D.J.L. Brett, Z.X. Guo, H. Wang, I.P. Parkin, Solid solution nitride/carbon nanotube hybrids enhance electrocatalysis of oxygen in zinc-air batteries, Energy Storage Mater. 15 (2018) 380–387. https://doi.org/10.1016/j.ensm.2018.08.020.

[29] K. Gong, F. Du, Z. Xia, M. Durstock, L. Dai, Nitrogen-Doped Carbon Nanotube Arrays with High Electrocatalytic Activity for Oxygen Reduction, Science 323 (2009) 760–764.

[30] S. Wang, L. Zhang, Z. Xia, A. Roy, D.W. Chang, J.B. Baek, L. Dai, BCN graphene as efficient metal-free electrocatalyst for the oxygen reduction reaction, Angew. Chemie - Int. Ed. 51 (2012) 4209–4212. https://doi.org/10.1002/anie.201109257.

[31] J. Zhang, Z. Zhao, Z. Xia, L. Dai, A metal-free bifunctional electrocatalyst for oxygen reduction and oxygen evolution reactions, Nat. Nanotechnol. 10 (2015) 444–452. https://doi.org/10.1038/nnano.2015.48.

[32] X. Liu, L. Dai, Carbon-based metal-free catalysts, Nat. Rev. Mater. 1 (2016) 16064. https://doi.org/10.1038/natrevmats.2016.64.

[33] J.-C. Li, P.-X. Hou, C. Liu, Heteroatom-Doped Carbon Nanotube and Graphene-Based Electrocatalysts for Oxygen Reduction Reaction, Small. 13 (2017) 1702002. https://doi.org/10.1002/smll.201702002.

[34] H.F. Wang, C. Tang, B. Wang, B.Q. Li, X. Cui, Q. Zhang, Defect-rich carbon fiber electrocatalysts with porous graphene skin for flexible solid-state zinc–air batteries, Energy Storage Mater. 15 (2018) 124–130. https://doi.org/10.1016/j.ensm.2018.03.022.

[35] J. Chen, Y. Zhang, M. Zhang, B. Yao, Y. Li, L. Huang, C. Li, G. Shi, Water-enhanced oxidation of graphite to graphene oxide with controlled species of oxygenated groups, Chem. Sci. 7 (2016) 1874–1881. https://doi.org/10.1039/c5sc03828f.

[36] Y. Zhang, B. Yang, K. Li, D. Hou, C. Zhao, J. Wang, Electrospun porous poly(tetrafluoroethylene-: Co -hexafluoropropylene- co -vinylidene fluoride) membranes for membrane distillation, RSC Adv. 7 (2017) 56183–56193. https://doi.org/10.1039/c7ra09932k.

[37] K. Ganesan, S. Ghosh, N. Gopala Krishna, S. Ilango, M. Kamruddin, A.K. Tyagi, A comparative study on defect estimation using XPS and Raman spectroscopy in few layer nanographitic structures, Phys. Chem. Chem. Phys. 18 (2016) 22160–22167. https://doi.org/10.1039/c6cp02033j.

[38] G. Zhang, S. Sun, D. Yang, J.P. Dodelet, E. Sacher, The surface analytical characterization of carbon fibers functionalized by H_2SO_4/HNO_3 treatment, Carbon 46 (2008) 196–205. https://doi.org/10.1016/j.carbon.2007.11.002.

[39] U. Zielke, K.J. Hüttinger, W.P. Hoffman, Surface-oxidized carbon fibers: I. Surface structure and chemistry, Carbon 34 (1996) 983–998. https://doi.org/10.1016/0008-6223(96)00032-2.

[40] J.K. Nørskov, J. Rossmeisl, A. Logadottir, L. Lindqvist, J.R. Kitchin, T. Bligaard, H. Jónsson, Origin of the overpotential for oxygen reduction at a fuel-cell cathode, J. Phys. Chem. B. 108 (2004) 17886–17892. https://doi.org/10.1021/jp047349j.

[41] G.L. Chai, Z.X. Guo, Highly effective sites and selectivity of nitrogen-doped graphene/CNT catalysts for CO2 electrochemical reduction, Chem. Sci. 7 (2016) 1268–1275. https://doi.org/10.1039/c5sc03695j.

[42] G.L. Chai, Z. Hou, D.J. Shu, T. Ikeda, K. Terakura, Active sites and mechanisms for oxygen reduction reaction on nitrogen-doped carbon alloy catalysts: Stone-wales defect and curvature effect, J. Am. Chem. Soc. 136 (2014) 13629–13640. https://doi.org/10.1021/ja502646c.

[43] J. Guo, S. Gadipelli, Y. Yang, Z. Li, Y. Lu, D.J.L. Brett, Z. Guo, An efficient carbon-based ORR catalyst from low-Temperature etching of ZIF-67 with ultra-small cobalt nanoparticles and high yield, J. Mater. Chem. A. 7 (2019) 3544–3551. https://doi.org/10.1039/c8ta10925g.

[44] X. Lu, O.O. Taiwo, A. Bertei, T. Li, K. Li, D.J.L. Brett, P.R. Shearing, Multi-length scale tomography for the determination and optimization of the effective microstructural properties in novel hierarchical solid oxide fuel cell anodes, J. Power Sources. 367 (2017) 177–186. https://doi.org/10.1016/j.jpowsour.2017.09.017.

[45] X. Lu, T. Li, A. Bertei, J.I.S. Cho, T.M.M. Heenan, M.F. Rabuni, K. Li, D.J.L. Brett, P.R. Shearing, The application of hierarchical structures in energy devices: New insights into the design of solid oxide fuel cells with enhanced mass transport, Energy Environ. Sci. 11 (2018) 2390–2403. https://doi.org/10.1039/c8ee01064a.

[46] H.L.K.S. Mosch, O. Akintola, W. Plass, S. Höppener, U.S. Schubert, A. Ignaszak, Specific surface versus electrochemically active area of the carbon/ polypyrrole capacitor: Correlation of ion dynamics studied by an electrochemical quartz crystal microbalance with BET surface, Langmuir. 32 (2016) 4440–4449. https://doi.org/10.1021/acs.langmuir.6b00523.

[47] Y. Sagara, A.K. Hara, W. Pavlicek, A.C. Silva, R.G. Paden, Q. Wu, Abdominal CT: Comparison of low-dose CT with adaptive statistical iterative reconstruction and routine-dose CT with filtered back projection in 53 patients, Am. J. Roentgenol. 195 (2010) 713–719. https://doi.org/10.2214/AJR.09.2989.

[48] P. Giannozzi, S. Baroni, N. Bonini, M. Calandra, R. Car, C. Cavazzoni, D. Ceresoli, G.L. Chiarotti, M. Cococcioni, I. Dabo, A. Dal Corso, S. De Gironcoli, S. Fabris, G. Fratesi, R. Gebauer, U. Gerstmann, C. Gougoussis, A. Kokalj, M. Lazzeri, L. Martin-

Samos, N. Marzari, F. Mauri, R. Mazzarello, S. Paolini, A. Pasquarello, L. Paulatto, C. Sbraccia, S. Scandolo, G. Sclauzero, A.P. Seitsonen, A. Smogunov, P. Umari, R.M. Wentzcovitch, QUANTUM ESPRESSO: A modular and open-source software project for quantum simulations of materials, J. Phys. Condens. Matter. 21 (2009) 3905502. https://doi.org/10.1088/0953-8984/21/39/395502.

[49] J.P. Perdew, K. Burke, M. Ernzerhof, Generalized gradient approximation made simple, Phys. Rev. Lett. 77 (1996) 3865–3868. https://doi.org/10.1103/PhysRevLett.77.3865.

[50] J.K. Nørskov, J. Rossmeisl, A. Logadottir, L. Lindqvist, J.R. Kitchin, T. Bligaard, H. Jónsson, Origin of the overpotential for oxygen reduction at a fuel-cell cathode, J. Phys. Chem. B. 108 (2004) 17886–17892. https://doi.org/10.1021/jp047349j.

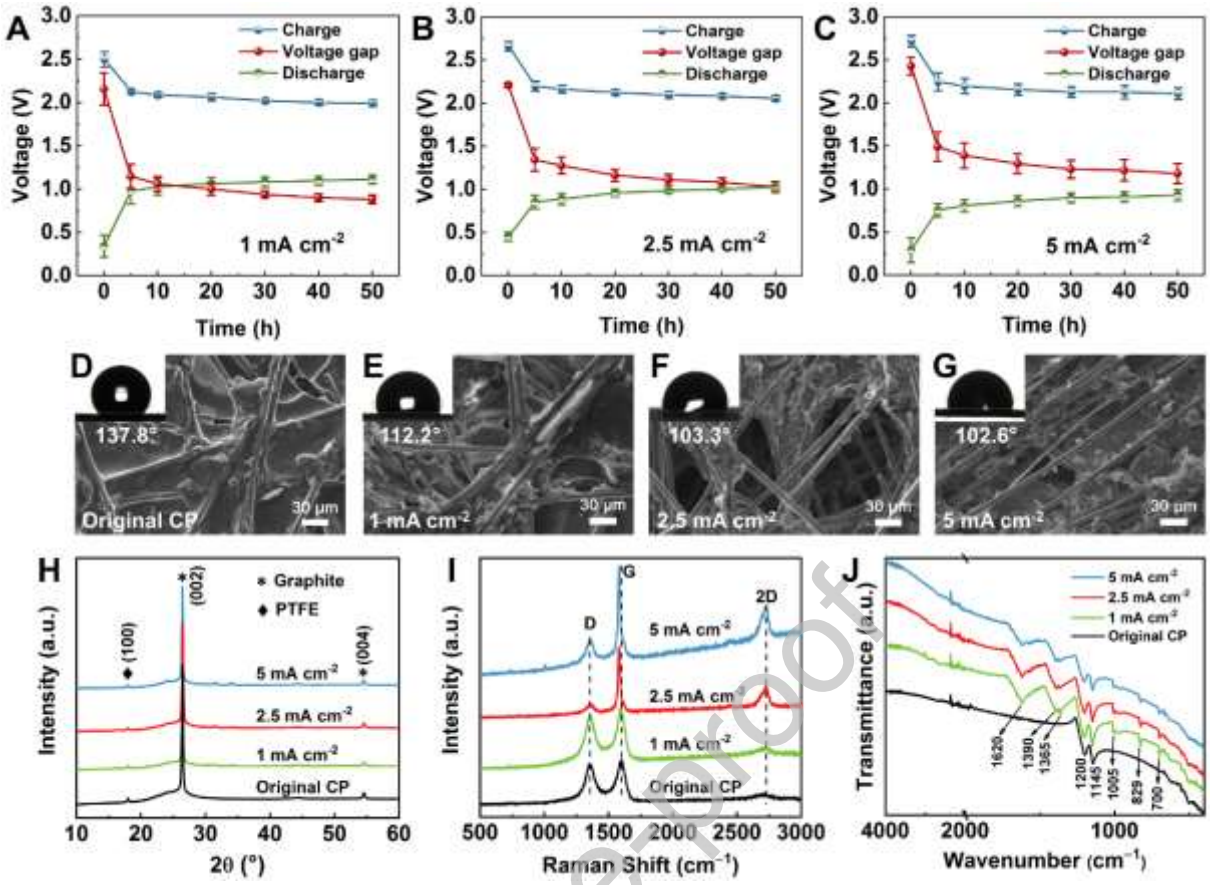

Fig. 1. Galvanostatic cycling performance and structural evolution of the CP. (A-C) Illustration of Zn-air batteries activated at the current densities of 1 mA cm^{-2} (A), 2.5 mA cm^{-2} (B) and 5 mA cm^{-2} (C), after 50 h discharge-charge cycling process, respectively. (D-G) SEM images of original CP and self-activated CP at different current densities (inset: corresponding contact angle). (H-J) XRD patterns (H), Raman spectra (I) and FTIR spectra (J) for original CP and self-activated CP at different current densities.

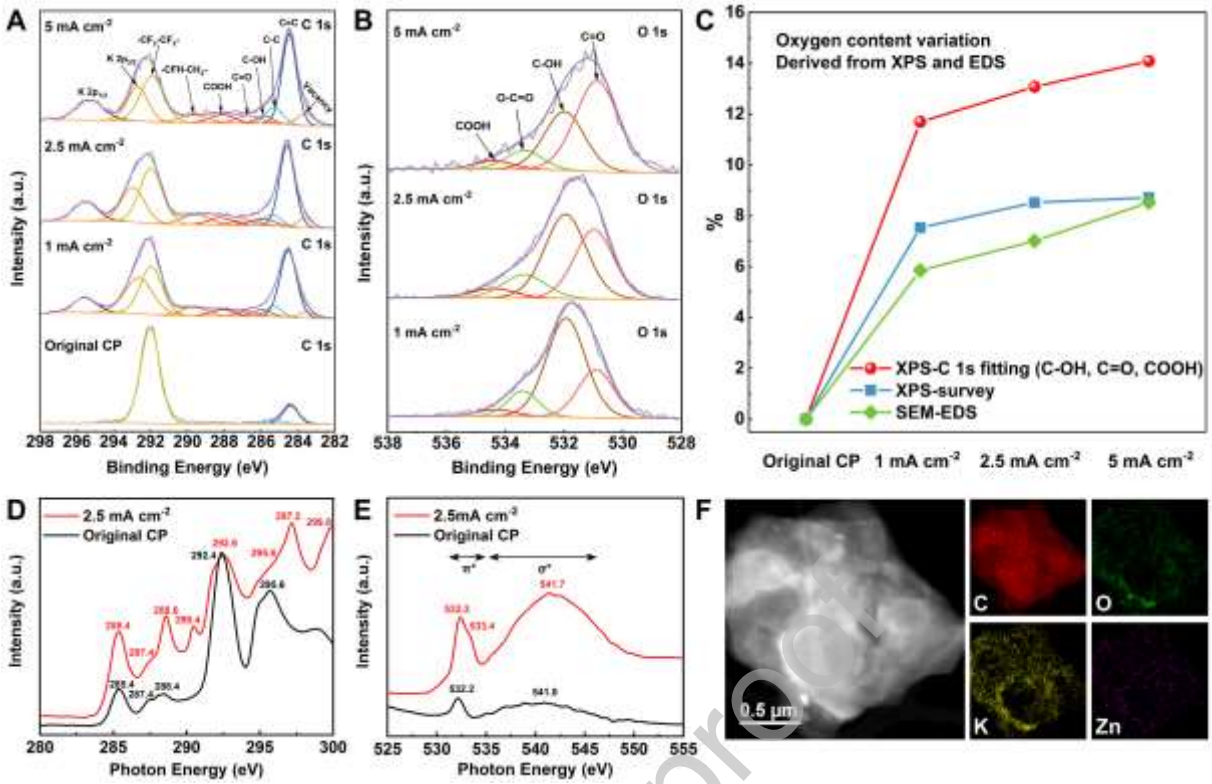

Fig. 2. Comparison of electrodes *via* structural and compositional characterizations. (A-B) High-resolution XPS spectra of C 1s (A) and O 1s (B) for original CP and self-activated CP at different current densities. (C) Oxygen content variation derived from XPS and EDS spectra. (D-E) C (D) and O (E) K-edge NEXAFS spectra for original CP and self-activated CP at a current density of 2.5 mA cm^{-2}. (F) HAADF–STEM image and the corresponding EDS elemental mapping of self-activated CP at 2.5 mA cm^{-2}.

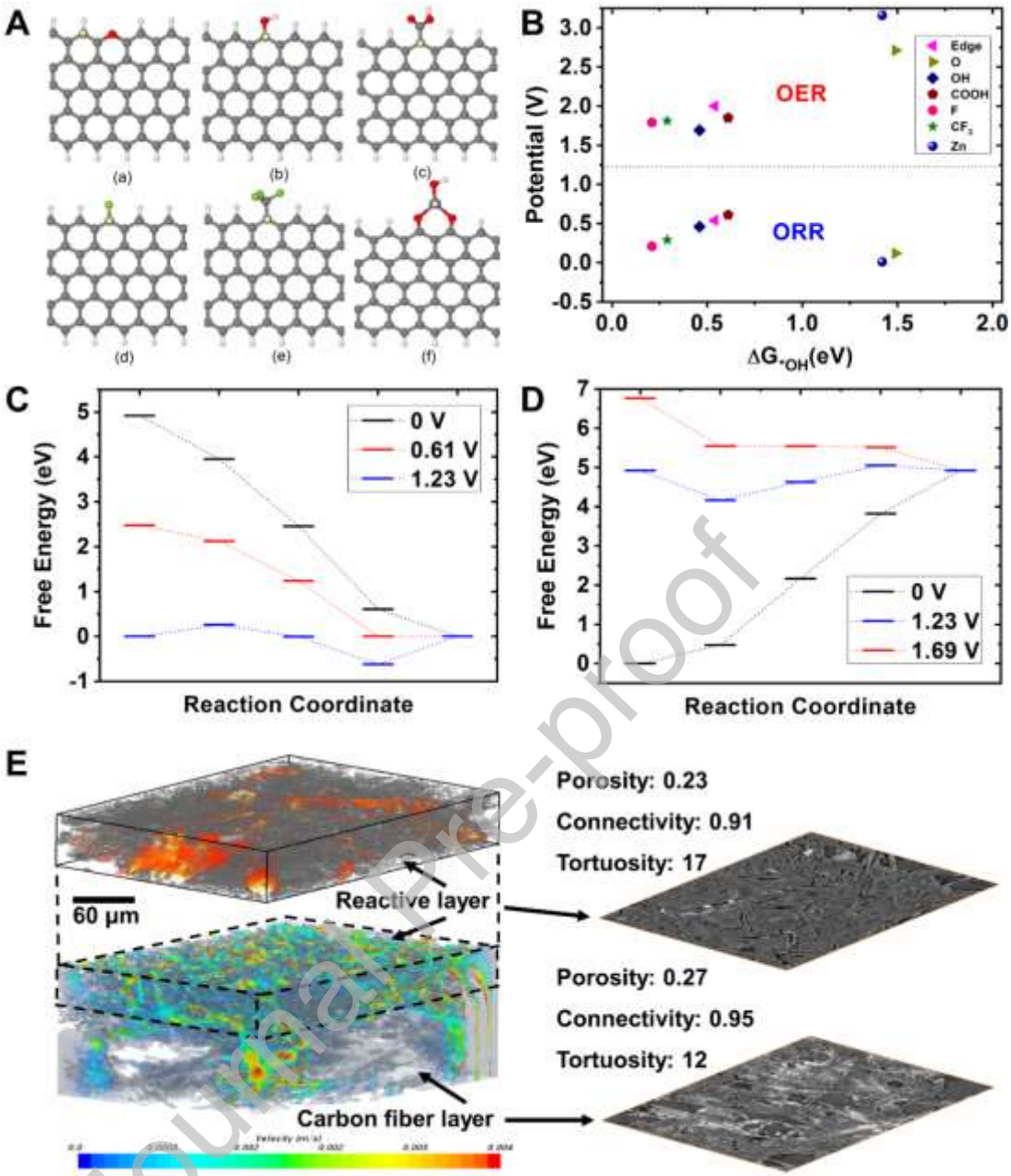

Fig. 3. Multiscale simulations from atomic to electrode scales. (A) Carbon material electrocatalysts with (a) –O group, (b) –OH group, (c) –COOH group, (d) –F group, (e) $–CF_3$ group, and (f) Zn related structures. The grey, white, red, green and silvery spheres denote for carbon, hydrogen, oxygen, fluorine and zinc atoms, respectively. The possible active sites studied are labelled in yellow colour. (B) The ORR/OER potentials for the studied structures. (C) The free energy variation for the ORR (discharge) process on carbon material electrocatalysts with –COOH group. (D) The free energy variation for the OER (charge) process on carbon material electrocatalyst with –OH group. (E) Computed fluid dynamics (CFD) simulation for self-activated CP at 2.5 mA cm^{-2}, the inlet is set as air with 1 bar and a reaction source is defined at the outlet equivalent to 3 mA.

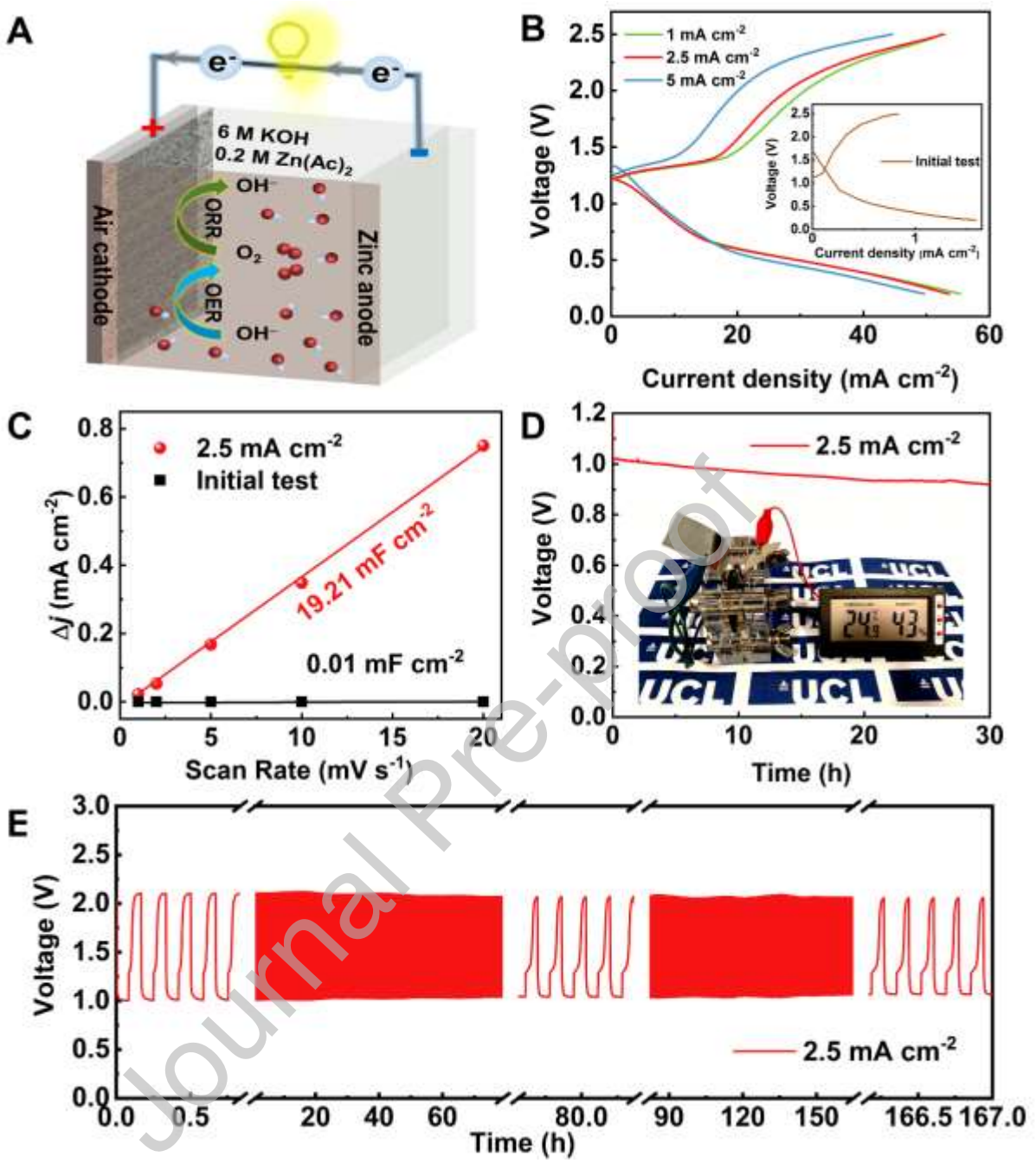

Fig. 4. Zn–air battery performance. (A) Schematic illustration of a ZAB. (B) Charge/discharge polarization curves of original CP and activated CP at different current densities. (C) Electrochemical surface areas of original CP and activated CP at 2.5 mA cm^{-2}. (D) Galvanostatic discharge curves of the ZAB using activated CP at 2.5 mA cm^{-2} as the cathode (inset: demonstration of one ZAB powering digital temperature and humidity indicator). (E) Cycling performance of the ZABs at 2.5 mA cm^{-2} (over 1000 cycles).